

Variable Density Turbulence Tunnel Facility

G. P. Bewley,¹ H. Nobach,¹ M. Sinhuber,¹ H. Xu,¹ and E. Bodenschatz¹

*Max Planck Institute for Dynamics and Self-Organization, Göttingen,
Germany*

(Dated: 3 December 2024)

The Variable Density Turbulence Tunnel (VDTT) at the Max Planck Institute for Dynamics and Self-Organization in Göttingen, Germany produces very high turbulence levels at moderate flow velocities, low power consumption and adjustable kinematic viscosity. To reach the highest Reynolds number, the tunnel can be filled and pressurized up to 15 bar with the dense gas sulfur hexafluoride (SF_6). The Reynolds number can be varied by changing the pressure or flow rate of the gas or by using different non-flammable gases including air. Turbulence is generated at the upstream ends of two measurement sections with grids, and the evolution of this turbulence is observed as it moves down the length of the sections. We describe the instrumentation presently in operation, which consists of the tunnel itself, classical grid turbulence generators, and state-of-the-art nano-fabricated hot-wire anemometers provided by Princeton University¹. We report measurements of the characteristic scales of the flow and of turbulent spectra up to Taylor Reynolds number $R_\lambda \approx 1600$, higher than any other grid-turbulence experiment. We also describe instrumentation under development, which includes an active grid and a Lagrangian particle tracking system that moves down the length of the tunnel with the mean flow. In this configuration, the properties of the turbulence are adjustable and its structure is resolvable up to $R_\lambda \approx 8000$.

PACS numbers: 47.27.-i, 47.27.nb, 47.27.nd, 47.27.Jv

I. INTRODUCTION

A. On the need for the VDTT

Turbulence plays a decisive role in the universe. Its influence extends broadly throughout nature and technology². For example, turbulence controls the spread of trace gases^{3,4}, pollutants⁵, and particulate matter⁶ in the atmosphere and oceans, the mixing of fuel and air in engines⁷, the generation of energy-draining wakes behind airplanes and cars⁸, and even the evolution of planets, stars and the universe as a whole^{9,10}.

What underlies all turbulent motion is the balance between the inertia of the fluid and the pressure and friction forces that the fluid exerts on itself. In almost every practical setting this balance is complicated by additional effects, such as buoyancy-driven convection where temperature gradients drive the flow¹¹, rotation-induced Coriolis accelerations in oceanic, atmospheric flows on earth or other planets¹², electromagnetic forces in conducting fluids like those that make up the sun¹³, nonlinear stresses in non-Newtonian fluids like blood¹⁴, or changes in material properties in flames¹⁵.

If we want to discover something generic about turbulence, something that is essential wherever turbulence is fundamental, we may limit our inquiries to its most essential ingredients: inertia, pressure, and friction. Such turbulence can be created by mechanically stirring a liquid or gas. In this spirit of interest in universality, we may also wish to exclude the influences of the geometry of the flow. We then want to study a flow that minimizes the effect of the boundaries of its container, and does not exhibit a preferred orientation¹⁶. Such a flow is called statistically homogeneous and isotropic¹⁷, and a close approximation of it can be realized in a wind tunnel by disturbing a uniform free-stream flow with a mesh or grid^{2,18}.

When turbulence is well-developed, it comprises large sweeping motions that contain most of the mechanical energy of the flow, and relatively small and sharp gradients that dissipate most of this energy¹⁹. The Reynolds number, $Re = \rho u' L / \mu$, gauges the separation between these large and small scales. In other words, high Reynolds numbers mean large scale separations. Here, ρ and μ are the density and dynamic viscosity of the fluid, respectively, u' is the amplitude of its velocity fluctuations, and L a characteristic scale over which motion is correlated. For typical values in the atmosphere, for example, the Reynolds number may

reach values of a million, or more.

Universal features of turbulence are expected to reveal themselves at high Reynolds numbers. That is, when the scale separation between the energetic and dissipative motions is large, and where at sufficiently small scales the flow may forget its initial conditions. Experiments at high Reynolds numbers are desirable, then, not only to gain insight into natural flows, but to provide clues about a fundamental description of turbulence. The question that remains is how to produce well-controlled, high-Reynolds-number turbulence whose properties are commensurate with current measurement technology.

The constraints in designing a facility to generate high-Reynolds-number turbulence are that it is realizable within the available space, time and funds, and that the turbulence it produces is observable with available technology. In this context, each of the density, viscosity, velocity and length scales must be optimized in order to maximize the Reynolds number. The fluctuating velocity and length scales u' and L determine the size of a facility and its power consumption. The fluctuating velocity, u' , is typically a fixed fraction of the mean flow speed, U , and the power required to run a facility scales with U^3 . Clearly, modest flow velocities and a modest size minimize both construction and operational costs. We are left to find a fluid with high density and low viscosity.

The VDTT uses pressurized gases to satisfy the requirement that the fluid density be high while the viscosity is low. Gases have low dynamic viscosities, μ , which depend only weakly on pressure. Thus the kinematic viscosity, $\nu = \mu/\rho$, can be decreased simply by increasing the pressure and thus the density ρ of the gas. The VDTT is equipped to use any non combustible gas, and Sulfur Hexafluoride (SF_6) in particular. SF_6 has the advantage that at atmospheric pressures it is 5 times denser than air, and at a pressure of 15 bar it reaches a density of about one tenth of water. This pressure is much lower than the 100 bar that would be needed to bring air to the same density. As a consequence, pressure vessels can be limited to 15 bar and can be built thin-walled and economically. By this method, the Reynolds number can not only be high, but can also be regulated over more than two decades by changing pressure alone. That is, without changing the conditions of the flow at the large scale; this translates to flexibility in controlling the experimental conditions. In addition, SF_6 has the advantage of not being hazardous to life other than by replacing air and the oxygen it contains. It has the disadvantage, however, of being a greenhouse gas; great care needs to be taken not to lose it to the environment.

The VDTT is a wind tunnel around which pressurized gases circulate in an upright, closed loop. At the upstream ends of two test sections in the VDTT, the free stream is disturbed mechanically. The resulting turbulence evolves down the length of the tunnel without the middle region being substantially influenced by the walls of the tunnel. The test sections are long enough (8 m) that the turbulence evolves through at least one eddy turnover time, $L/u' \approx 1$ s, during its passage down the tunnel. That is, the turbulence can be observed over the time it takes energy to cascade from the large scales all the way down to the dissipative ones.

The width of the cross section of the tunnel constrains the characteristic scale L of the flow, and for fixed L higher Reynolds numbers lead to ever smaller scales of motion. In the VDTT, the cross section is wide enough (1.5 m) that even at the highest Reynolds numbers, the smallest scales of motions are neither too small nor too fast to be resolved by existing state-of-the-art instrumentation. We note that scales of a modest size are also desirable if one wants to use optical techniques to resolve all scales of the flow. With current technologies large optical components, like lenses, mirrors and detectors, are difficult to produce.

The VDTT was designed around a Lagrangian particle tracking system (LPT). This requirement implies a limit on the mean flow rate U . The VDTT's maximum flow speed of $U = 5$ m/s is sufficiently small that we can accelerate the LPT system to match the flow speed at the upstream end of the test sections, move it at mean-flow speed down the tunnel, and stop them at the downstream ends. We can then follow the evolution of the flow in the frame of the flow itself, by imaging the motions of particles carried by the flow. Eulerian measurements are not excluded, and the data we present here were acquired with both traditional hot wires and the new NSTAP probes²⁰. These were the constraints on the design of the VDTT.

The history of using pressurized gases goes almost back 100 years. We therefore provide in the remainder of this introduction a short historical review of predecessors to the VDTT. That is, of wind tunnels in which the density of the working fluid could be varied. There are several other types of wind tunnels and a great variety of turbulence facilities in general that we do not review, and which are worthy of an article in and of themselves. We continue in Section II with a description of the apparatus and its technical details. In section III, we describe velocity measurements and their statistics, and we conclude with an outlook in Section IV.

B. Historical Review of Variable Density Facilities

Variable density wind tunnels have been an important tool for aeronautical research and development for almost 100 years. Since both the density and the speed of the wind in such tunnels could be adjusted independently, both the Reynolds number and the Mach number of the flows could be set independently. This made it possible with small-scale models to observe the aerodynamics of full-scale airplanes under well-defined laboratory conditions. Before the advent of computers, these tunnels provided the *only* way to test design ideas. We emphasize that even with today’s computers, wind tunnel tests remain essential in the development of airplanes. In the following, we give the maximum Reynolds numbers attainable in the various facilities in terms of its mean flow speed and 10% of its width, so that $Re_{WT} \equiv 0.1\sqrt{AU}/\nu$, where A is the cross sectional area of the tunnel.

The first wind tunnel in which the density of the working fluid could be adjusted was the “Variable Density Wind Tunnel of the National Advisory Committee for Aeronautics” (VDT, with one “T” instead of two). It was designed by Max Munk²¹, a student of Ludwig Prandtl in Göttingen. The latter was also the founder of the Kaiser Willhelm Institute for Flow Research, which is the predecessor of the MPI for Dynamics and Self-Organization. The VDT was built at the Langley Research Center in Virginia and became operational in 1923. As must be the case in all pressurized wind tunnels, the gas in the tunnel went around a closed circuit rather than being open to draw air in from the surrounding environment. Recirculating tunnels such as the VDT are called Göttingen-type tunnels²². The test section of the VDT was housed in a 10.2 m long, 4.6 m wide cylindrical pressure vessel that could withstand pressures up to 21 atm²³. The tunnel was used to test airfoils and model airplanes in states corresponding to various atmospheric conditions. The original tunnel was made of wood, and was destroyed by a fire in 1927. It also faced serious difficulties with vibration and flow quality, so that the tunnel was redesigned as a more rigid and fire-proof structure when it was rebuilt in 1930²⁴.

The VDT produced a huge amount of airfoil data, reaching Reynolds numbers of about $Re_{WT} = 5.4 \cdot 10^6$. But high free-stream turbulence intensities led to inaccurate measurements of drag. To overcome this problem, the “Langley two-dimensional low-turbulence pressure tunnel” (LTPT) was designed and completed in 1938, also at the Langley Research Center²⁵. The LTPT was large, at 44.5 m long and 17.7 m wide. By design, the airfoils in this tunnel

could span the whole test section, effectively reducing by one the dimension of the flow. The tunnel ran at pressures up to 10 atm and at Reynolds numbers of up to about $Re_{WT} = 6.1 \cdot 10^6$. A low turbulence level of less than 1% was achieved through a contraction with a large area ratio in combination with a series of wire screens. This tunnel was operational for many years and underwent massive modifications in the early 1980's²⁶. It was still in operation during the early 21th century²⁷ until the drive motor burned in 2006. Demolition of the tunnel began after no further funding for repair was granted. Further information can be found on the NASA website²⁸.

Several years after the construction of the original VDT, interest in variable density tunnels spread over to Europe. This can be seen in the construction of the “Compressed Air Tunnel” at the National Physical Laboratory in Teddington in 1931²⁹. In its 6 foot diameter test section, air could be compressed up to 25 atm to produce a wide range of Reynolds numbers up to $Re_{WT} = 8 \cdot 10^6$. As with the VDT, the main focus of the Compressed Air Tunnel was the aerodynamical improvement of aircraft.

A different approach to model testing was chosen in Braunschweig with the construction of the “Variable density high speed cascade wind tunnel” at the Deutsche Forschungsanstalt für Luftfahrt in 1956. In this tunnel, the pressure could be lowered from 1 to 0.1 atm to test the performance of blade cascades under various conditions. The Reynolds and Mach numbers in the tunnel could be set independently,³⁰ up to a maximum Mach number of 1.1 and Reynolds number $Re_{WT} = 4 \cdot 10^6$.

While there were several experiments focused on airfoils or model planes in variable density wind tunnels, relatively few exist that addressed fundamental turbulence questions. The first was probably a study of Kistler and Vrebalovich, which reports on classical grid turbulence experiments at the “Southern California Co-operative Wind Tunnel”³¹ just before it closed in the 1960's³². The measurements were made at wind speeds of up to 60 m/s and with air pressures between 0.2 atm and 4 atm. The size of the cross section was 2.6 m \times 3.5 m, so that Reynolds numbers up to $Re_{WT} = 4.5 \cdot 10^6$ were possible. The observed turbulence produced by classical grids, so that the grid Reynolds number $Re_M = \rho U M / \mu$ is relevant, where M is the mesh spacing of the grid. The combination of high pressure, high velocities, and large cross section allowed for measurements of both the decay and the spectra of grid turbulence at grid Reynolds numbers up to 2.4 million, higher than any previous study, or indeed than any subsequent study. The grid turbulence data we introduce in this paper

are the first to exceed in Reynolds number those of Kistler and Vrebalovich; we reach 4.9 million.

A second series of fundamental studies in pressurized tunnels was conducted at the Nuclear Research Laboratories in Jülich in the 1970's. The wind tunnel there could be filled with Helium of up to 40 bar. While the main focus of the facility was heat transfer in heat exchangers for power plants, some work was done on the flow past spheres³³. Here, the Reynolds numbers reached $Re_{WT} = 3.1 \cdot 10^5$.

A relatively recent facility is the “high pressure wind tunnel” (HDG) at the German Aerospace Center (DLR) in Göttingen³⁴. The HDG withstood pressures up to 100 bar and ran at speeds of up to 35 m/s, so that Reynolds numbers up to $Re_{WT} = 1.3 \cdot 10^7$ were possible. It has seen extensive use in studies of models and of physical effects such as flow-induced resonances³⁵. For example, the classical problem of flow around a circular cylinder was investigated in the range $10^4 < Re < 10^7$ merely by varying the flow parameters and not the size of the cylinder^{36,37}.

In the late 1990's, the Princeton/DARPA-ONR SuperPipe Facility was built at the Princeton Gas Dynamics Lab Facilities. It is a 34 m long and 1.5 m wide pipe flow facility with a 12.9 cm test section diameter. It circulates air pressurized to between 1 and 220 atm³⁸, so that Reynolds numbers reached $Re_{WT} = 2.3 \cdot 10^6$. This highly pressurized air made it possible to uncover the scaling laws of pipe flows at very high Reynolds numbers, $Re^+ = Ru_\tau/\nu$, of about 10^5 . Here R is the radius of the pipe and ν/u_τ the viscous length scale³⁹.

To allow for model testing, a grant for a wind tunnel based upon the SuperPipe Facility was granted in 1998 and led to the construction of the Princeton/ONR High Reynolds Number Testing Facility. This wind tunnel operates at up to 240 bar. With two 2.6 m test sections of 46 cm diameter, it allows for submarine model testing at high Reynolds numbers up to $Re_{WT} = 9.6 \cdot 10^6$. A more detailed description of this and the SuperPipe facility can be found on the website of the Princeton Gas Dynamics Lab Facilities⁴⁰.

II. CONSTRUCTION DETAILS

The facility at the Max Planck Institute in Göttingen comprises a pressure vessel, associated gas handling apparatus, safety systems, grids to generate turbulence, and turbulence

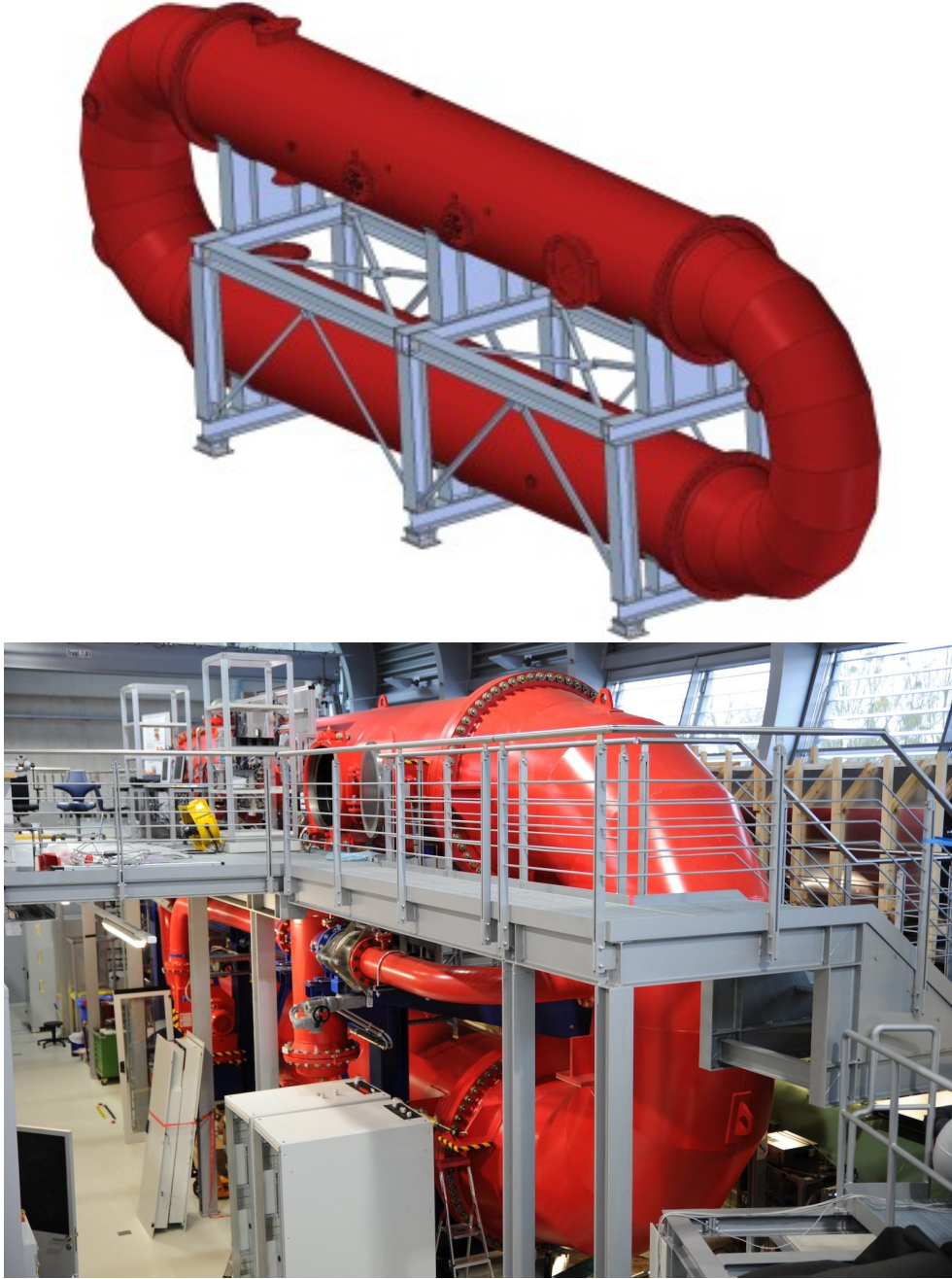


FIG. 1. 3D view and photograph of the Variable Density Turbulence Tunnel.

measurement systems. We describe these systems in some detail in the following sections. We also describe some of the measures undertaken to control the homogeneity of the flow in the measurement sections in Sec. II J.

A. Pressure Vessel

As can be seen in Fig. 1, the pressure vessel is upright, 18.2 m long, and 5.3 m high. It consists of two 11.68 m long straight cylindrical sections with an inner diameter of 1.84 m, and two elbows with a center-line radius of 1.75 m and an inner diameter of 1.52 m. The total volume of the pressure vessel is 88 m^3 , which corresponds to 8.7 t of SF_6 at 15 bar and 20°C . The pressure vessel is made of P265GH (1.0425) steel, the straight tubes are 20 mm thick, and two elbows are 18 mm thick. The support frame is made of S 235 JRG2 steel. To reduce mechanical coupling between the tunnel and the building, the tunnel rests on three vibration isolated foundations (Fig. 3).

Mechanical access to the interior of the pressure vessel is possible both by removing the elbows, and through three manholes. Two of the manholes are on the sides of the two straight measurement sections (Fig. 4). These manholes are 0.8 m diameter and have quick-lock mechanisms to make it easy to open and close the tunnel. The additional manhole is placed in one of the elbows (see Fig. 6) to allow access to the space between the fan in the lower part and the heat exchanger in the upper part of the wind tunnel. This manhole is 0.6 m in diameter. To access the full cross section of the straight sections, the two elbows (Fig. 5) can be removed with a movable frame (Fig. 6). To ensure precise docking and undocking of the flanges between the elbows and the straight sections, the last few centimeters of the movement are controlled by four hydraulic cylinders (Fig. 7).

The main flanges connecting the two elbows of the tunnel to the straight sections and the manholes all use re-usable O-ring seals. The tunnel's main flanges use double O-rings in rectangular grooves to minimize leakage, the manholes at the measurement sections use single O-rings in rectangular grooves, and the manhole at the bend uses a single O-ring in an trapezoidal groove. All other seals are kammprofile gaskets. The maximum leak rate of the pressure vessel and all connected parts of the entire facility are specified to be better than 0.5 % of their respective volumes per year.

B. Working Fluids

The wind tunnel can be filled and operated with any non-corrosive gas. We have so far used air, nitrogen and SF_6 , but other gases are possible. At room temperature and pressure,

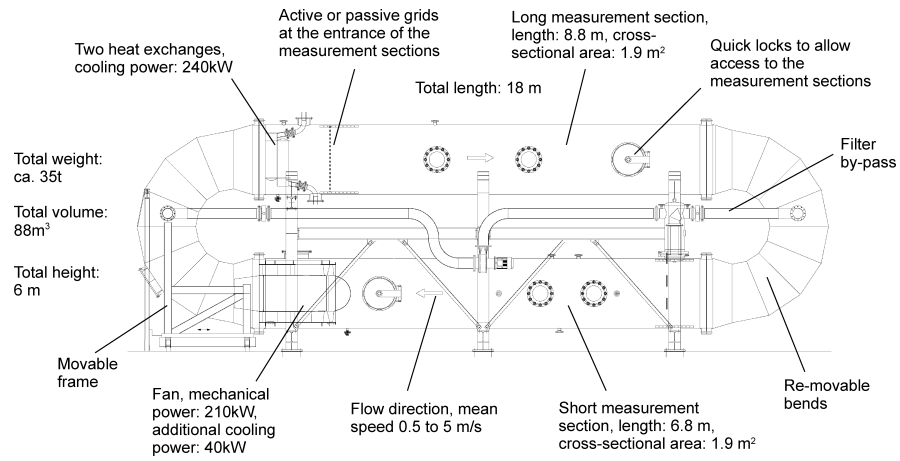


FIG. 2. Sketch of the VDTT.

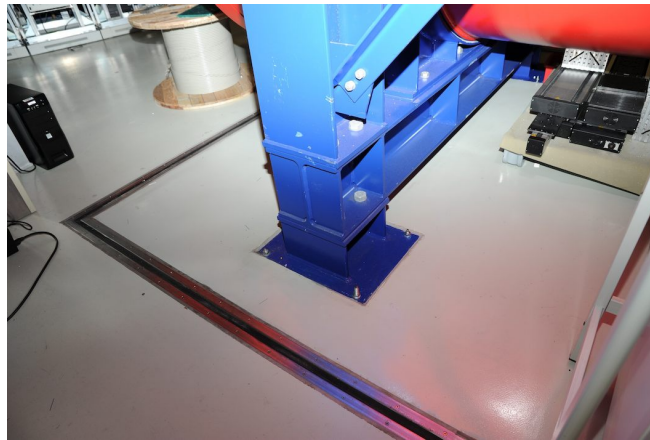


FIG. 3. Vibration isolating foundation. There is one of these under each of the three supports on which the VDTT rests.



FIG. 4. Manhole at the end of one of the two measurement sections. Its diameter is 80 cm.



FIG. 5. One of two elbows is removed and reveals the cross section of the tunnel.

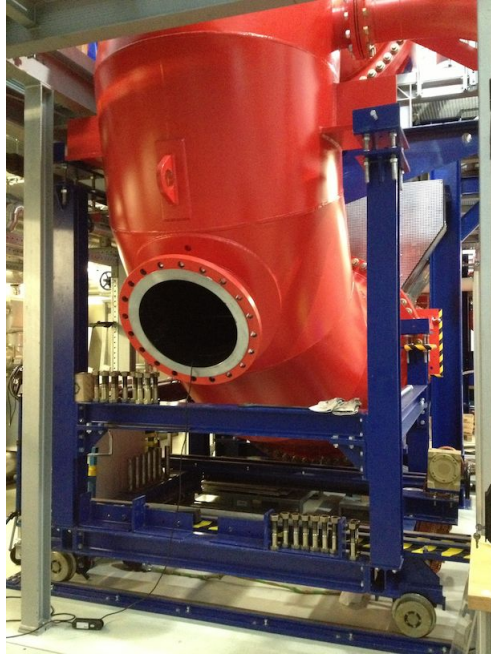


FIG. 6. Additional manhole to access the space between the fan and the heat exchanger, and the frame on rails that supports the elbow when it is being moved.

SF_6 has a density of $\rho = 6.52 \text{ kg/m}^3$ and a kinematic viscosity of $\nu = 2.32 \times 10^{-6} \text{ m}^2/\text{s}$. These values change to $\rho = 112 \text{ kg/m}^3$ and $\nu = 0.143 \times 10^{-6} \text{ m}^2/\text{s}$ at 15 bar⁴¹ making it possible to access a wide range of Reynolds number by changing the pressure alone. SF_6 is an inert gas, but decomposes above 1200 °C⁴², though this temperature can be lower on catalytic surfaces, like certain metals.



FIG. 7. Hydraulic cylinders control the docking and undocking maneuvers of the elbows.

C. Gas Handling System

The facility includes an automated gas handling system (Fig. 8). The system supplies the wind tunnel with SF_6 and other gases including dried air. The SF_6 is stored in the liquid phase in tanks (Fig. 9). The system both evacuates and pressurizes the pressure vessel. It also gasifies, liquefies, and cleans SF_6 .

The typical cycle to prepare the wind tunnel for a run starts by closing the vessel to evacuate it. The evacuation is performed to minimize the amount of residual air in the tunnel. Once a pressure of 1 mbar has been reached, the tunnel is filled with the desired gas up to 15 bar. The system can maintain a given pressure during measurements. When SF_6 is used, and after the run is complete, the system pumps the gas back to the storage tanks, and reduces the pressure in the vessel to 1 mbar. The vessel is then filled again with air to 1 bar and opened.

D. Safety System

All components of the facility have appropriate safety systems. This safety equipment includes over-pressure valves and burst plates, which prevent pressures so high that they could damage parts of the system. To avoid the contamination of the laboratory space with SF_6 , all safety valves open into a pipe that ends outside the building. In addition, all components of the system have sensors that detect malfunctions and can shut down the entire system. For example, there is a sensor that shuts the motor down if the temperature



FIG. 8. Gas-handling system, including a vacuum pump and two compressors.



FIG. 9. Storage tanks, in which the SF_6 is stored in liquid form.

inside the wind tunnel exceeds 40°C .

The pressure vessel itself has a safety release system consisting of a burst plate and a safety valve (Fig. 10) that limits the operational pressure to 15 bar. At this pressure the burst plate first breaks without releasing any SF_6 through the safety valve. Next, a gauge that monitors the pressure in the space between the burst plate and the safety valve indicates an overpressure. Only if the pressure increases beyond 19 bar does the safety valve release the gas from the pressure vessel. The wind tunnel itself is certified up to 20 bar, and the operational pressure can be increased up to that value, provided the safety release system is redesigned in such a way that an evacuation of the gas is guaranteed, even when there is energy being injected into the system by, for example, the motor. There is a similar safety release system on the filter bypass (described in the next section), which opens at



FIG. 10. Burst plate and safety valve with pressure monitor and exhaust pipe.

19.5 bar. Each of the two safety valves are connected with pipes that open outside the building. Flexible couplers are installed between the valves and the pipes in order to allow for vibration and misalignment.

During maintenance or installation of experimental equipment the safety of persons working in the wind tunnel must be guaranteed. Therefore, after an experiment and after the pressure vessel is again filled with air, the manholes are opened and the gas handling system is decoupled from the pressure vessel by double block-and-bleed valves (Fig. 11). These are two valves in series blocking the gas supply pipe from the pressure vessel, and one valve opening the space between the two valves to release to the environment any gas that leaks. Furthermore, the wind tunnel is actively ventilated while open, and persons working in the wind tunnel carry O_2 detectors. Finally, portable SF_6 detectors are used to locate leaks and to check the SF_6 concentration in the pressure vessel before entering it.

The experimental hall itself and the SF_6 storage room are both equipped with fire, SF_6 and O_2 detectors linked to a centralized alarm that initiates an evacuation in all dangerous situations. These alarms are also linked to the fire department in order to get fast and professional help in the case of dangerous situations.

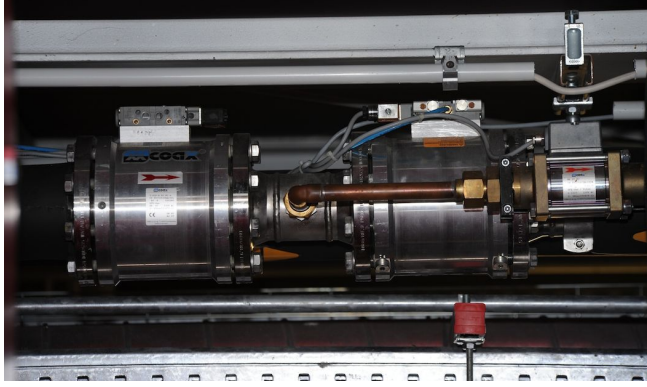


FIG. 11. Double-block-and-bleed valves in the gas supply line.

E. Filter Bypass

The wind tunnel is equipped with a bypass to clean the gas in the pressure vessel. A pump draws gas from one elbow (see Fig. 2), pushes it through a class F9 filter to remove particles from the gas, and returns it to the other elbow. The F9 filter efficiency is 98% for 1 micron particles. The bypass itself is a 19 m long tube (Fig. 12) with an inner diameter of 250 mm. The flow rate through the bypass is up to $400 \text{ m}^3/\text{h}$. To avoid leaks the pump is entirely encapsulated, its connection to an external motor made through a magnetic coupling. To compensate for mechanical stresses caused by differences in the expansion of the bypass and the main body of the pressure vessel, the filter bypass includes two flexible couplers (Fig. 13). The expansion is due to temperature or pressure fluctuations. To prevent pressure-driven flow through the filter bypass during measurements, the bypass can be closed with any of three valves along its length. Since the gas in the bypass can be enclosed by any pair of valves, an additional safety release consisting of a burst plate and a safety valve with pressure monitoring was necessary here.

F. Fan

The pump that recirculates the gas in the wind tunnel is a 210 kW electric motor coupled to a fan with 20 blades. There is a stator with 17 blades, and the annular passage through both fan and stator has an inner diameter of 0.935 m and an outer diameter of 1.5 m. Both fan and motor are inside the pressure vessel, in the downstream end of its lower section. The flow is ducted into the fan by guide plates upstream of the fan. The fan speed is controlled



FIG. 12. Filter by-pass line with magnetically coupled pump (middle) and F9 filter cassette (end).

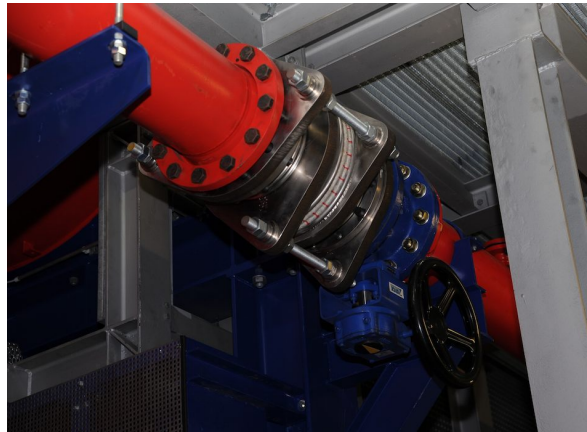


FIG. 13. One of two flexible couplers along the filter by-pass line.

by a frequency controller, yielding a constant mean flow velocity that is adjustable between 0.5 m/s and 5 m/s with SF_6 at 15 bar.

The motor is housed to prevent particles added to the flow from causing damage to the

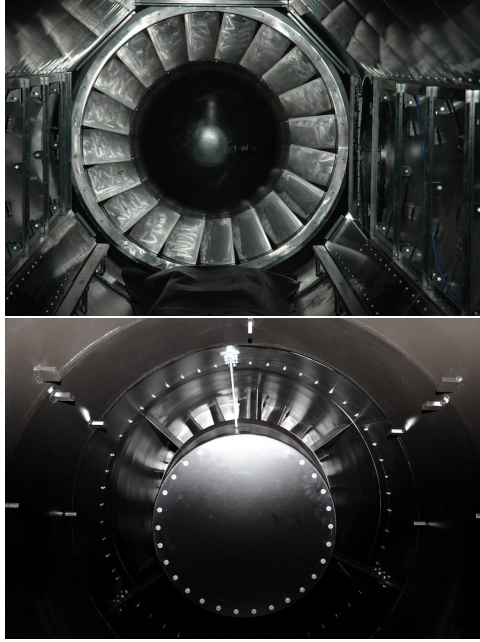


FIG. 14. Fan (looking downstream) and encapsulated motor (looking upstream) in the lower measurement section.

bearings. The motor is water cooled, with 40 kW cooling power available from the main cooling system of the facility. The cooling water for the motor is driven by a dedicated pump to ensure the minimum required flow rate necessary to cool the motor. If there were a leak in the cooling system, SF_6 could leak into it. Should this happen, the pressure increase in the system would be detected and valves in the cooling lines would close automatically.

Although housed, the motor is exposed to the full range of pressures in the tunnel between vacuum and 20 bar. For this reason, the motor coils were specially made to be insulated by a bubble-free coating. This to prevent expansion of the bubbles that would damage the insulation.

The motor temperature and vibration are monitored. The motor controller shuts the motor down when any problems are detected. All connections to the motor are made through leak-tight feedthroughs.

G. Heat Exchanger

A heat exchanger inline with the flow removes the heat generated by pumping, *i.e.* all of the mechanical energy put in by the fan. The heat exchanger consists of two water-cooled

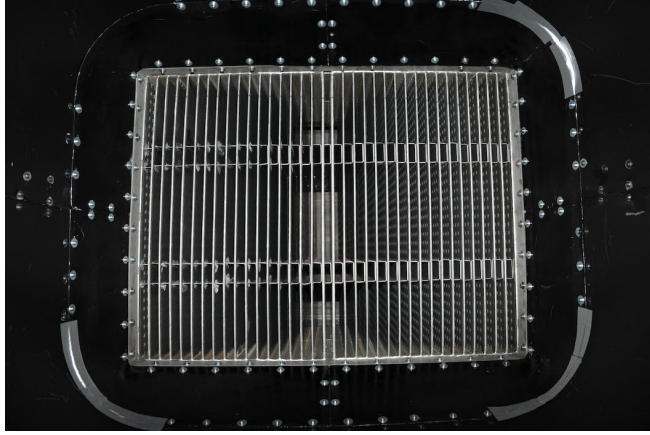


FIG. 15. Heat exchanger (looking downstream). Water flows through the vertical plates that we see here end-on, while the black shrouds guide the SF_6 through the heat exchanger.

registers stacked in series. Each of these registers is 245 mm long and 1.268 m wide and consists of 36 vertical plates, as can be seen in Fig. 15. The inside height is 0.96 m. The plates are 5 mm thick with an open space of 28 mm between each plate. An earlier version of the heat exchanger suffered from aeroelastic resonances, which were suppressed by the addition of U-shaped spacers in the open space between the plates. The heat exchanger is centered with respect to the wind tunnel. The flow is guided from the elbow into the heat exchanger by shrouds, so that there is no flow around the heat exchanger.

The incoming cooling water flows through one half of the heat exchanger (18 plates), gets collected, turns back and flows through the other half of the heat exchanger. To avoid temperature gradients over the tunnel's cross-section, the cooling water flows through the two heat exchangers in the same rotational orientation but the two heat-exchangers are rotated by 180° with respect to each other.

To achieve maximum efficiency, the heat exchanger is connected directly to the cooling water system of the building; there is no additional heat exchanger. The two registers of the heat exchanger receive the same constant flow rate, which is driven by a common pump. The temperature controller holds constant the fluid temperature to set points between 20°C and 35°C . This is realized by mixing cold water from the building with hot water from the heat exchanger return flow. Since this causes a varying flow rate in the support line from the building, an additional pump on the building side in combination with an excess flow valve realizes a constant flow rate on the building side.

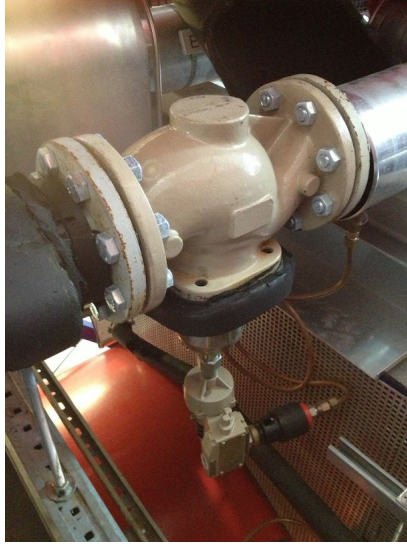


FIG. 16. Safety valves in the cooling water pipes.

Since the cooling water is at the nominal pressure of the building, there is a pressure difference across the surfaces of the heat exchanger. The heat exchanger is designed to sustain the full pressure difference between the cooling water and the pressure inside the wind tunnel (between vacuum and maximum 20 bar absolute). The cooling water flows to the heat exchanger through feedthroughs that on one side are flexible enough to accommodate deformations due to temperature and pressure variations, and on the other side are stiff enough to withstand the full pressure difference between the pressure of the cooling water system inside and the wind tunnel pressure on the other side.

To prevent SF_6 from penetrating the cooling water system of the building in the case of a leak in the heat exchanger, the cooling water supply pipes include two valves that close at a pressure of 4 bar over the nominal. An additional four valves (see Fig. 16) close at an over-pressure of 6 bar. In the case of a leak, first the pressure in the building system increases, which causes the two valves in the supply pipes to close and isolate the building side of the cooling system. Then the pressure continues to increase until the four valves at the wind tunnel close in order to enclose the SF_6 in the wind tunnel.

In the case of a leak of water into the tunnel, a conductive humidity sensor placed below the heat exchanger initiates an alarm and shuts down both the wind tunnel driver and the cooling system.

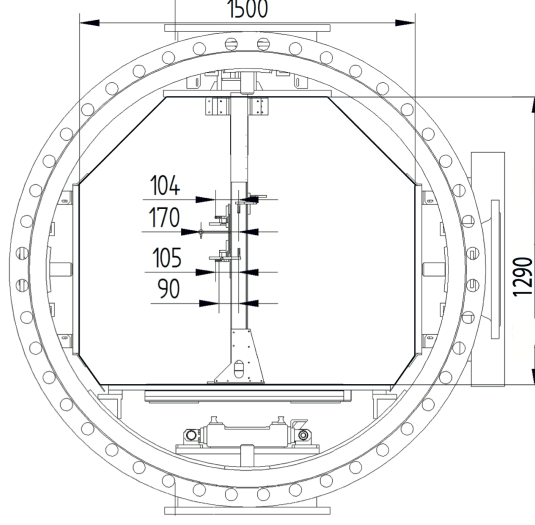


FIG. 17. Cross section of the wind tunnel. Also shown is the linear traverse that held the hot wires, discussed below. Dimensions in *mm*.

H. Measurement Sections

The long straight sections of the pressure vessel contain the measurement sections. The wind flows through interior ducts, or wind tunnels, as seen in cross section in Fig. 17. The width of the tunnels are about 1.5 m, their heights are about 1.3 m, and the corners of their cross sections are cut off to make them approximately octagonal. The tunnels have a cross-sectional area of 1.7 m^2 , which slightly increases downstream through the inclination the roof by 0.114° and the side walls by 0.057° in the upper measurement section, and 0.110° and 0.055° , respectively, in the lower measurement section. The upper measurement section is 8.8 m long, and the lower one 6.8 m long.

At the upstream end of each test section, there are four mounts, one each on the top, bottom, left and right sides, to which turbulence generators can be mounted. Each mount can withstand forces up to 10 kN continuously in the direction of the flow, and transients up to 22.5 kN in the case of an accident. At the end of the 8.8 m long upper measurement section a shroud adapts the cross section of the measurement section to the circular profile of the elbow. The same is true at the entrance of the lower measurement section. All inner parts of the wind tunnel are painted black to minimize reflections in optical measurements.

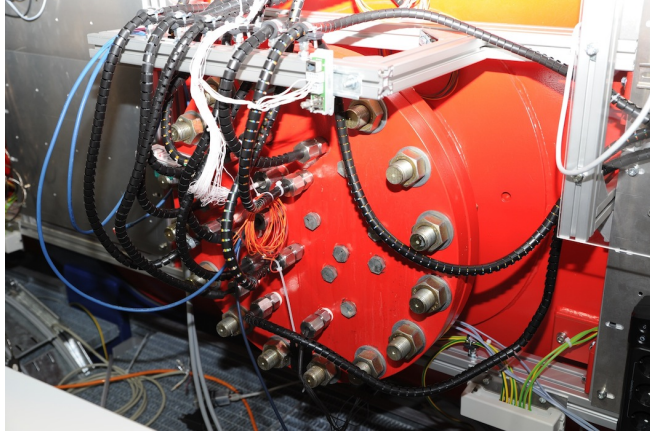


FIG. 18. Flange with multiple 3/4" Conax NPT feed-throughs with up to 60 wires each.

I. Electrical and Optical Access

To connect electrical probes and other electrical equipment inside the wind tunnel with the outside, we use electrical feed-throughs. For this reason, each of the two measurement sections have two 400 mm flanges onto which plates with tapped holes are mounted. Each plate has 21 3/4" NPT taps. Depending on the required current through the wires, different kinds of feedthroughs with different numbers of wires and different wire diameters have been installed. Up to 60 signal wires can pass through each 3/4" NPT tap (see Fig. 18).

Optical access to high-pressure devices is generally difficult to implement. The VDTT has two borosilicate glass windows with an open diameter of 50 mm with a direct view into the wind tunnel (see Fig. 19). The outer diameter of the glass is 107 mm, with thickness 20 mm. To prevent the catastrophic release of SF_6 through a broken window, there are ball valves between the pressure vessel and the glass windows. These ball valves close automatically when there is a flow through the flange. The trigger for the ball valves to close is the detection of a pressure difference between the flange and the interior of the tunnel, which is zero unless there is a flow through the flange.

Aside from these two windows, optical access also is possible through optical fibers, which pass through feedthroughs. A 150 W Nd:YAG laser has been coupled into such a fiber for illumination of the test section for optical particle tracking.

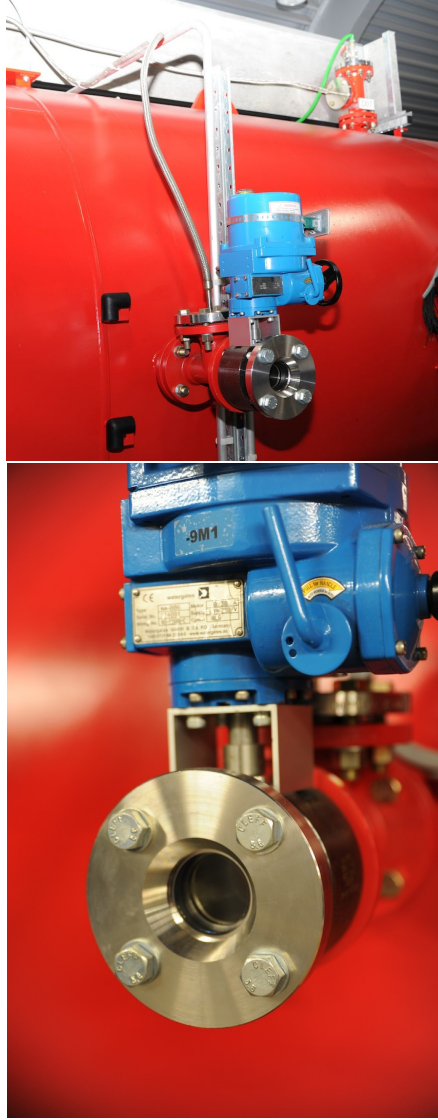


FIG. 19. One of two optical access windows with ball valve and dynamic pressure monitoring.

J. Aerodynamic Considerations

Here we describe in general terms the character of the flow as it circulates through the tunnel. One of our main interests was to produce a homogeneous flow in the measurements sections. Residual inhomogeneity of the flow is set by the tunnel geometry upstream of the sections. The flow is sustained by the fan described in section II F, where it will acquire some rotation depending on the fan speed, since the stator has a fixed geometry. Thereafter, the flow passes through the elbow described in section II A. The elbows contain no vanes to guide the flow. There are, however, mounting flanges in the elbows so that guide vanes can

be installed if required. As described by Görtler⁴³ and Hawthorne⁴⁴, oscillating secondary flows probably emerge in these elbows due to their curvature.

The flow then enters the heat exchanger (Section II G) through a contraction with an area ratio of 1.5 that smoothly adapts the circular cross section of the elbow to the rectangular cross section of the heat exchanger. From the point of view of the flow, the heat exchanger consists of vertical slots. These slots destroy large-scale vortical structure. We observed, however, that the flow exited more quickly from the top of the heat exchanger than from the bottom of it.

Between the heat exchanger and the entrance to the upper measurement section is an 800 mm long expansion that adapts the cross section of the heat exchanger, which has an area of 1.2 m^2 , to the cross section of the measurement section, which has an area of 1.7 m^2 (Fig. 17). As can be seen in Fig. 20, the walls of the expansion consist of flat plates, so that separation can occur at the corners along the inlet edge of the expansion. We observed this separation with telltales and cameras. In order to stabilize and homogenize the flow in the expansion⁴⁵, we added screens at approximately 250 mm intervals along the length of the expansion. The meshes had the following properties, in the order encountered by the flow: wire diameter in mm/wire mesh spacing in mm: 0.4/0.850, 0.4/1.267, 0.5/2.833.

As described below in Sec. II K, grids at the upstream end of the measurement sections produced turbulence. The grids are 545 mm downstream of the last screen in the expansion described above. The absence of large scale rotation in the flow in the test section was checked with a swirl meter. A more detailed view of the quality of the flow in the test sections can be found in Section III.

After the upper measurement section, the flow turns in the elbow, and returns to the fan through the lower measurement section. Between the elbow and the lower measurement section are a section that adapts the cross section of the elbow to that of the measurement section, and a bank of wire-mesh screens with properties similar to the ones in the expansion upstream of the upper measurement section. Note that there is no heat exchanger, nor expansion upstream of the lower measurement section.

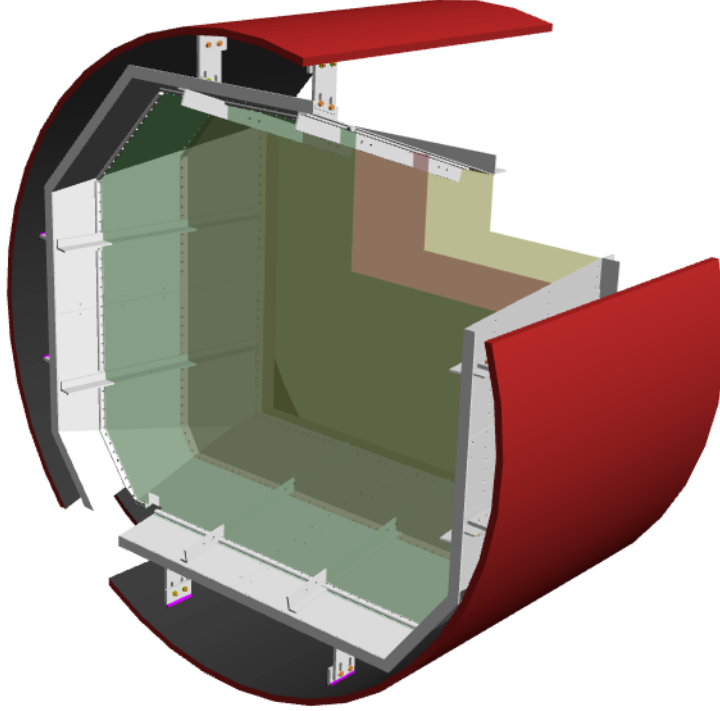


FIG. 20. Drawing of the expansion between the heat exchanger and the upper measurement section. The flow emerges from the face of the expansion in this view, so that the flow goes from right to left. The screens are shown as colored planes, with a cut-out for improved visibility.

K. Grids

We introduce here an active grid that we designed for the VDTT, and which is under development. We also describe the classical grids that we employed to produce the turbulence we characterize in the next section.

Active grids were developed only recently as a way to generate in wind tunnels high-Reynolds number flows with convenient properties⁴⁶. Active grids work by stirring the flow with rotating paddles, rather than disturbing it through the wakes of stationary bars, as in a classical grid. Modern active grids generate not only high-Reynolds number flows, but also flows with tailored properties⁴⁷. Such control is desirable where turbulence with certain statistical properties is needed, as is the case when the atmospheric boundary layer needs to be synthesized to observe its effect on wind turbines⁴⁸, or where the effects of variation of the large-scale properties of the turbulence on the small-scale dynamics need to be understood⁴⁹. Since the large-scales are created by the geometry of the apparatus in an experiment, one

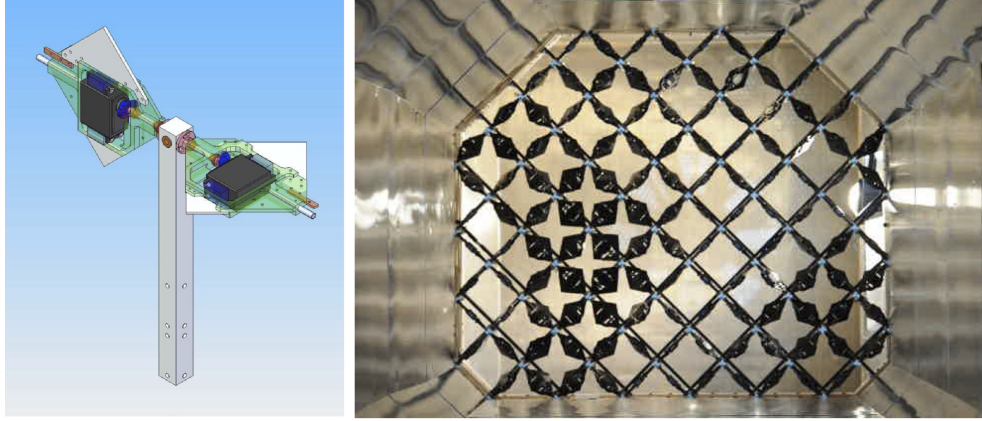


FIG. 21. On the left is a computer rendering of two active-grid paddles, each with its own integrated servo motor. 129 such paddles compose the active grid, seen face-on in the right panel. Here, the paddles are at various angles to the flow, in some places blocking the flow more than in others. The grid is shown here installed in the Prandtl tunnel, which is itself shown in Fig. 22 below.

advantage of the active grid is that its geometry is variable and can be adjusted during its operation. In this way, the response of the turbulence to changes in the properties at the large scales can be measured.

Our active grid advances active grid technology because there are many more degrees of freedom in the motions of its paddles than in previous grids. There are 129 degrees of freedom, whereas others had about 20. This gives an unprecedented level of control over the turbulence generated by the grid. Each degree of freedom corresponds to a single diamond-shaped paddle, the collection of which tile the cross section of the tunnel. Each paddle has its own computer-controlled servomotor that adjusts the angle of the paddle relative to the mean flow about an axis perpendicular to the flow. The paddles block the flow locally to a degree that depends on the angle of the paddle. The paddle angles can change over time according to some algorithm programmed by the user.

The active grid is presently being tested in an open-return wind tunnel built originally in the Kaiser-Wilhelm Institute of Ludwig Prandtl by Fritz Schulz-Grunow from 1936-1938. As seen in Fig. 22, the test section is 10 m long, with a cross section identical to the one in the VDTT. The maximum flow speed in the tunnel is approximately 11 m/s.

To make the measurements presented in this paper, we installed classical grid turbulence generators at the upstream end of the upper measurement section. We used one of three grids



FIG. 22. The Prandtl tunnel sits parallel to the VDTT with a cross section identical to the one inside the VDTT. Most easily visible here, at the left side of the picture, is the outlet of the tunnel, with a linear traverse that holds hot wire probes. The wooden frames and sheet metal walls were built in 2011. The inlet and fan in the background, at the top right of the picture, are the parts built nearly 80 years ago.

of traditional construction¹⁸. They were composed of crossed bars with square cross sections in two layers, with the vertical bars being upstream of the downstream ones (Fig. 23). The distances between the bars of each grid were 53.3 mm, 106.6 mm and 186.6 mm. The grid bars had widths 10 mm, 20 mm and 40 mm, respectively, so that the grids blocked about 34%, 34% and 38% of the area of the cross section. The grids were designed to have a distance of about a half mesh spacing between the wall and the first bar on each of the bottom, top, left and right sides. As in Bewley⁵⁰, we found that the flow profile was sensitive to the precise geometry of the intersection between the grid and the wall. Because of this, we adjusted the width of the bars closest to the top and bottom walls in order to optimize the homogeneity of the flow in the center of the tunnel.

L. Traverses

Within the VDTT, measuring instruments such as cameras will move down the length of the tunnel at the mean speed of the flow. This way, it is possible to follow the motions of particles within the turbulence, rather than sampling the flow as it sweeps past a fixed position. That is, one can view turbulence from the Lagrangian, rather than Eulerian,

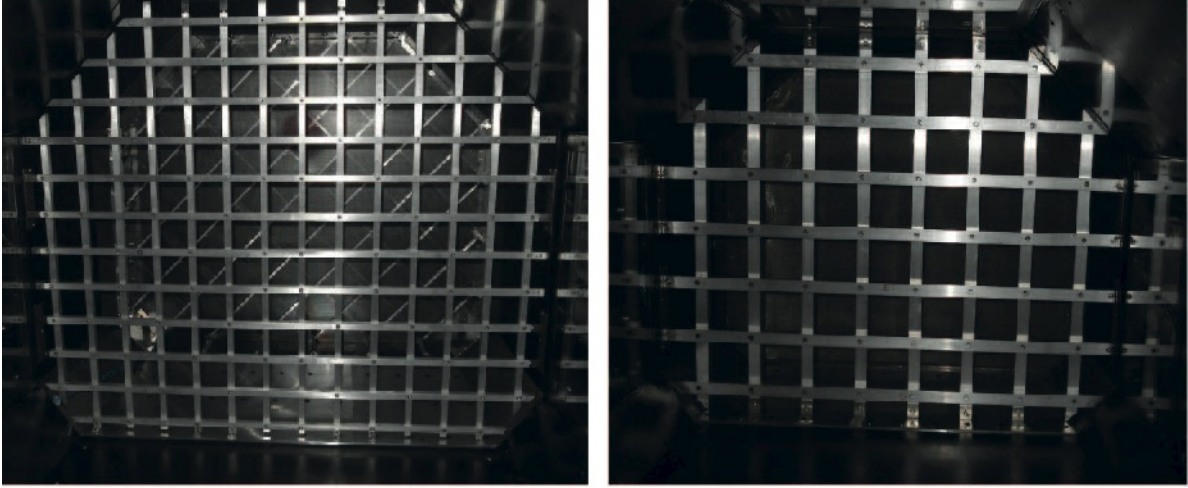


FIG. 23. Two of the classical grids we used to excite turbulence at the upstream end of the upper measurement section. Here, we look upstream at the 106.6 mm grid on the left, and the 186.6 mm on the right. Behind the 106.6 mm grid is another diagonal grid and screen that we installed to control the flow, and which we subsequently removed.

perspective. The basic idea is that cameras take movies of particles that are suspended in the flow. A laser light source illuminates the particles. From views acquired by multiple cameras, software determines the three-dimensional positions of the particles at a series of instants, and then reconstructs their tracks through three-space over time⁵¹. To accomplish this, the measurement sections accommodate movable sleds weighing up to 350 kg that are driven by linear motors. The sleds will carry cameras, optics, and other instruments at the mean velocity of the circulating gas, up to 5 m/s. There are few comparable installations^{52–54}, and none on the scale of the VDTT. The alignment of the cameras, the focusing of the lenses and the calibration of the imaging system will be performed automatically within the pressure vessel.

A prototype of the linear motor for the wind tunnel has been built and is presently being tested outside of the tunnel. The platform, onto which high-speed cameras are installed, is driven back and forth along high-precision, low-friction rails by an electrical linear motor. The 88 kW linear motor delivers up to 7.6 kN of force to accelerate a payload (cameras and optics) at one end of the tunnel, carry them along the length of the tunnel, and decelerate them at the other end. A linear encoder that has an accuracy of $0.2\ \mu\text{m}$ controls the position and the velocity of the platform.

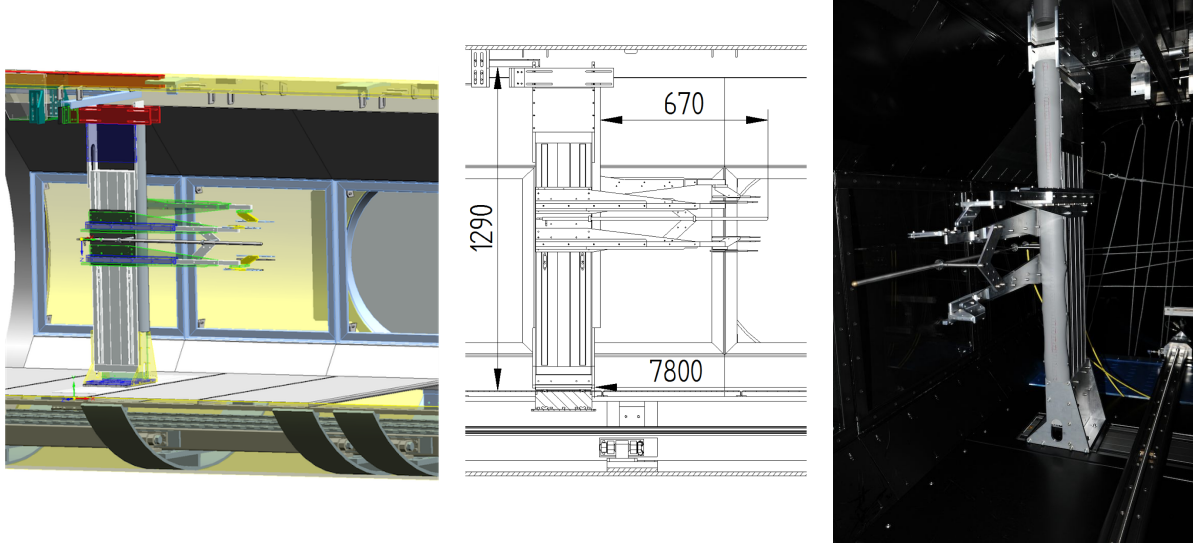


FIG. 24. Traverse mount for hot-wires, temperature sensors and Pitot-static tubes. Dimensions in *mm*. The distance of 7800 mm in the center panel is measured to the face of the grid. See also Fig. 17.

As in most wind tunnels, measurement equipment can otherwise be mounted anywhere along the measurement sections. Devices can be mounted directly to the walls, or on linear traverses.

The probes for the test measurements presented below were mounted on a 2D traverse, manufactured by Isel, to allow measurements at different fixed positions in the cross-section of the tunnel, and at a single distance from the grid (Fig. 24). The traverse moved 0.65 m in the horizontal direction and 0.60 m in the vertical. The tips of the Pitot tube and the hot-wire probes were about 0.77 m upstream of the face of the traverse. The parts supporting the probes were designed according to the rule of thumb that the width of the part be about ten times smaller than distance of the part from the probe. This was to minimize the flow distortion caused by the probe supports, while still providing the stability needed to minimize probe vibration. For some of the measurements, one probe was held at a fixed height, so that the distance between it and the probes moving up and down on the vertical traverse could be varied. We did this to measure correlations between velocities spaced across the tunnel.

M. Measurement Systems

The arsenal of diagnostic equipment familiar in fluid mechanics can be used in the VDTT. We have developed designs to incorporate hot wire anemometry, cold wire thermometry, laser Doppler velocimetry, acoustic velocimetry, particle sizing, dynamic pressure measurement, Particle Image Velocimetry (PIV), and Lagrangian Particle Tracking (LPT). The latter option will be implemented on the linear traverse mentioned above.

The system employed to acquire the data in this paper was a Dantec StreamLine hot wire anemometry system. We used two kinds of Dantec wires, with $2.5\,\mu\text{m}$ diameter and $450\,\mu\text{m}$ length, and with $5\,\mu\text{m}$ diameter and $1\,\text{mm}$ length. We also used the new NSTAP probes developed at Princeton²⁰, which were either $30\,\mu\text{m}$ or $60\,\mu\text{m}$ long. The probes were calibrated in situ against Prandtl (or Pitot-static) tubes while varying the fan speed. We used X-wires with $2.5\,\mu\text{m}$ wires to measure the Reynolds stresses, whose angular responses were calibrated with the Dantec calibrator using air at standard temperature and pressure. The signals were filtered at $30\,\text{kHz}$ and sampled at $60\,\text{kHz}$ with a digital acquisition card.

III. TEST EXPERIMENTS

We measured the characteristics of the turbulence at a fixed distance, $7.1\,\text{m}$, from the $186.6\,\text{mm}$ classical grid, and on a array of 150 points covering a $60\,\text{by}\,60\,\text{cm}$ square centered in the cross section of the tunnel. The measurements were made in both air and SF_6 at different pressures between $1\,\text{bar}$ and $15\,\text{bar}$. The profiles of the flow were measured by Dantec hot wires, and the spectra by NSTAPs.

Table I summarizes the properties of the turbulence. These properties were calculated as follows. The energy dissipation rate was extracted from the third order structure functions using the $4/5^{th}$ law, $D_{LLL}(r) \approx -\frac{4}{5}\epsilon r$ in the inertial range, so that our practical definition of it was $\epsilon = \max(-\frac{5}{4}D_{LLL}(r)/r)$. Here $D_{LLL}(r) = \langle \delta u^3(x, r) \rangle_x$ is the third moment of the longitudinal velocity differences, $\langle \cdot \rangle_x$ is the average over x , $\delta u(x, r) = u(x + r) - u(x)$ are the velocity differences, u , x , and r are parallel, and we used Taylor's hypothesis to extract x and r from the time series of each probe. We are aware that this measure of the dissipation rate is smaller than the actual dissipation rate at low Reynolds numbers. The measure becomes more accurate as the Reynolds number increases⁵⁵. This has the effect,

TABLE I. The flow parameters for the passive grid experiments. P is the pressure of the gas in the tunnel, ρ and ν are the density and viscosity of the gas, respectively, U is the mean speed of the flow, u'/U is the turbulence intensity, L is the streamwise longitudinal integral scale, ϵ is the dissipation rate per unit mass, η and τ_η are the Kolmogorov length and time scales, respectively, λ is the Taylor scale, and R_λ is the Taylor Reynolds number.

fluid	Air	SF ₆	SF ₆	SF ₆	SF ₆	SF ₆
P [bar]	1.0	1.1	2.1	4.0	12	15
ρ [kg/m ³]	1.20	6.52	12.6	25.1	85.3	112
ν [mm ² /s]	15.2	2.32	1.21	0.602	0.184	0.143
U [m/s]	4.31	4.16	4.11	4.11	4.08	4.08
u'/U [%]	2.35	3.33	3.38	3.28	3.50	3.70
L [mm]	148	139	151	125	125	123
ϵ [cm ² /s ³]	66.0	163	166	159	181	203
$\epsilon L/u^3$	0.58	0.71	0.83	0.77	0.77	0.75
η [μm]	930	170	100	61	24	19
τ_η [ms]	61	13	9.1	6.3	3.2	2.6
λ [mm]	22.5	6.71	4.77	3.26	1.76	1.53
$Re_{WT} \times 10^{-3}$	43	260	510	1000	3400	4400
R_λ	150	400	549	730	1370	1620

among others, of slightly inflating the value of the lower Reynolds numbers. The amplitude of the velocity fluctuations is $u' = \langle u^2 \rangle_x^{1/2}$. The integral scale, L , is the integral of the longitudinal correlation functions, $L = u'^{-2} \int_0^\infty \langle u(x+r)u(x) \rangle_x dr$, and we used exponential extrapolations to extend the integrals to infinity⁵⁶. The Taylor scale was evaluated through the isotropic relation, $\lambda = (15\nu \langle u^2 \rangle_x / \epsilon)^{1/2}$. Since the turbulence was approximately isotropic at all scales⁵⁶, the Reynolds number is given by $R_\lambda = u'\lambda/\nu$. The Kolmogorov scales are given by $\eta = (\nu^3/\epsilon)^{1/4}$, and $\tau_\eta = \sqrt{\nu/\epsilon}$, as usual.

Observe in Table I that changing the Taylor Reynolds number by an order of magnitude has only a small effect on the integral measures of the flow, u' and L . The effect on the dissipation rate is also small. The main effect of Reynolds number variation is on the scale at which dissipation occurs, a point that we revisit below.

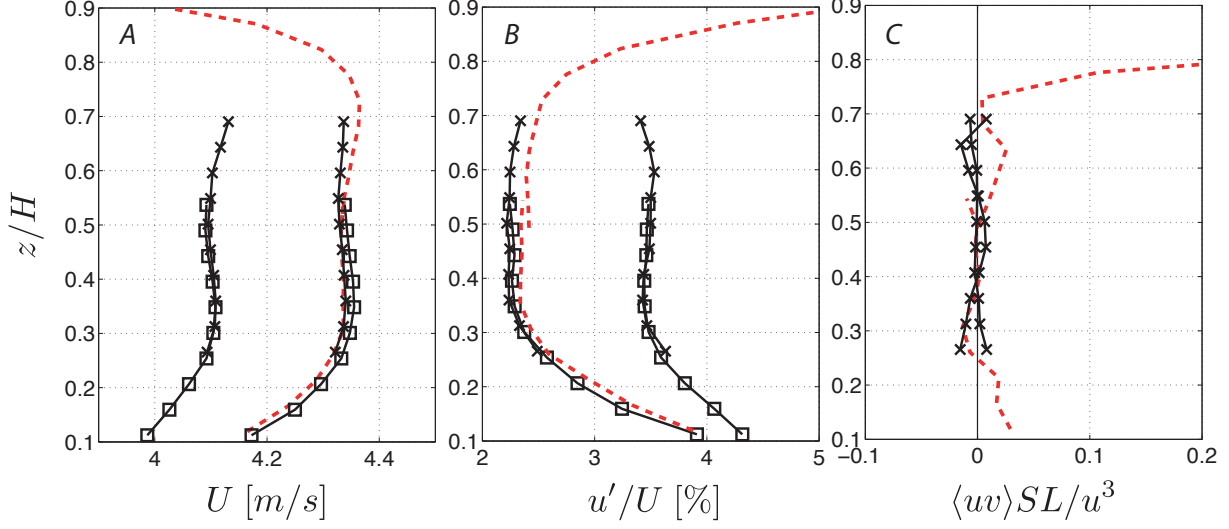


FIG. 25. A. Profile of the mean velocity as a function of vertical distance from the floor of the tunnel. The vertical position z is normalized by H , the distance from the floor to the ceiling. The \times symbols were acquired with an X-wire, and the \square symbols with a single wire. The dashed red curve was acquired separately in air with X-wires mounted on a traverse that made a wider range in z accessible. B. Profile of the turbulence intensity as a function of vertical distance from the floor of the tunnel. C. Profile of the turbulence production by shear as a fraction of the dissipation rate. For all of these measurements, the rotation rate of the fan was 20 Hz, while its maximum is 24.5 Hz so that mean flow speeds up to about 5.3 m/s are possible.

In the sections that follow we describe the statistics of the flow at positions midway between the side walls, and at various distances, z/H , from the floor of the tunnel, where z is the height of the probe above the floor and H is the height of the tunnel. Horizontal cuts, made across the width of the tunnel, were at least as good, or better, than the vertical cuts we present, in the sense that the deviations from homogeneity across the width were smaller. We then discuss the properties of the spectrum of the velocity fluctuations. Some analysis of these data, namely of conditional structure functions, has already been published in Blum et al.⁴⁹.

A. Profile of Mean Velocity

Fig. 25A shows the profile of the mean velocity, U , as a function of vertical distance from the floor of the tunnel. The shape of the profile was independent of the viscosity of the gas. The mean velocity was approximately constant across the middle half of the section, though there were boundary layers at the top and bottom of tunnel as well as a small velocity deficit near $z/H = 0.5$. As mentioned in Section II K, the width of the boundary layers may be related to the way the edge of the grid meets the wall of the tunnel. The boundary layers were slightly thinner when we used grids with smaller mesh spacing. Despite these features, the mean flow is reasonably uniform between z/H values of 0.25 and 0.75. The mean flow was slower at higher pressures, which may indicate that the pump was less efficient there than at lower pressures.

B. Profile of Turbulence Intensity

Fig. 25B shows the profile of the turbulence intensity u'/U in %. As with the mean flow, the turbulence intensity is approximately constant between z/H values of 0.25 and 0.75. The anisotropy in the fluctuations, u'/v' , where u' was in the streamwise direction and v' was in the spanwise direction, was between 1 and 1.1, so that the fluctuations were slightly stronger in the streamwise direction, as has been observed in grid turbulence before¹⁸. The turbulence intensity increased with Reynolds numbers for reasons that we do not know, though the same phenomenon was observed also in the HDG at the DLR in Göttingen (described above). We speculate that the turbulence decays more slowly at high Reynolds numbers, and are now performing experiments to test this idea.

C. Profile of Turbulence Production by Shear

Fig. 25C shows the profile of the turbulence production by shear, $\langle uv \rangle SL/u'^3$, as a fraction of the energy dissipation rate. Here, u and v are the velocity fluctuations in the streamwise and spanwise directions, respectively, $\langle uv \rangle$ is the Reynolds stress, $S = \Delta U/\Delta z$ is the mean shear rate and is derived by taking finite differences of the data in Fig. 25A, and u'^3/L is a measure of the energy dissipation rate per unit mass, ϵ . The production of turbulence by shear is negligible, being of the order of about 1% of the turbulence dissipation rate within

the center part of the flow. Its importance increases as expected in the top and bottom boundary layers.

D. Reynolds-stress Anisotropy

To quantify the the Reynolds-stress anisotropy, we plot the two invariants of the anisotropic Reynolds stress tensor $\langle u_i u_j \rangle - \frac{1}{3} \langle u_k u_k \rangle \delta_{ij}$ on the so-called Lumley triangle^{57,58}. We assume that the two transverse components are statistically the same, *i.e.*, $v' = w'$, and $\langle vw \rangle = 0$. We compare the Reynolds-stress anisotropy of the turbulence in the VDTT with other laboratory flows, including: the von Kármán swirling flow between counter-rotating disks (“the French washing machine”)⁵⁹, the Lagrangian Exploration Module (LEM)⁶⁰, and the “soccer-ball”⁶¹. The data for the French washing machine and the LEM were obtained using three-dimensional particle tracking⁵¹, while the data for the soccer-ball were measured with laser-Doppler velocimetry and similar assumptions on the two transverse velocity components were used to construct the Reynolds stress tensor. As shown in Figure 26, the turbulence produced in the VDTT was closer to isotropic than all other flows. The degree of isotropy increased with Reynolds number.

E. Turbulence Spectra

Figure 27 shows the development of the inertial range in the energy spectra through extension of the small scales. These are 30 micron NSTAP data in air and 1, 2, 4, 12 and 15 bar SF₆, and the measurements were made in the center of the tunnel where the flow was approximately homogeneous. The spectra, $E_{11}(k_1) = \int \int_{-\infty}^{\infty} \frac{E(k)}{2\pi k^2} \left(1 - \frac{k_1^2}{k^2}\right) dk_2 dk_3$, are normalized by the integral quantities, u' and L , which change only a little with Reynolds number, as can be seen in Table I. The collapse of the spectra at large scales supports the view that the dynamics at these scales are Reynolds number independent. In other words, they are controlled by the mean flow speed and the geometry of the grid, and are not strongly influenced by the material properties of the gas. This shows that our device works in the sense that we control the large scales and modulate the small scales by changing the pressure.

Fig. 28 compares a spectrum acquired with a Dantec probe to one with an NSTAP at

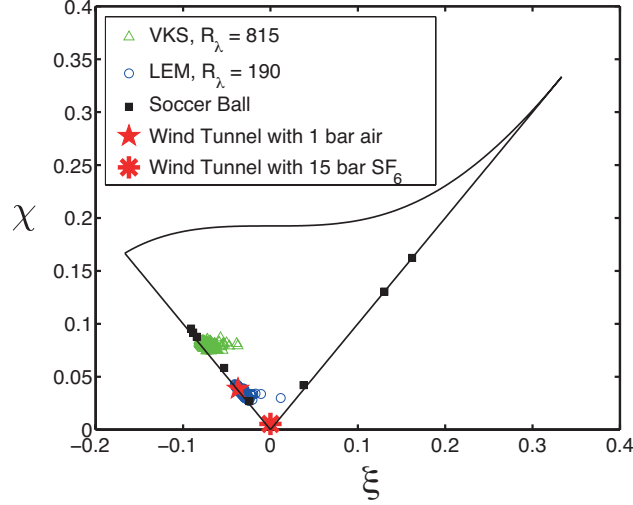


FIG. 26. Comparing Reynolds-stress anisotropy on the Lumley triangle. Here ξ and χ are two independent invariants of the Reynolds-stress anisotropy tensor $b_{ij} = \langle u_i u_j \rangle - (1/3)\langle u_k u_k \rangle \delta_{ij}$, defined as $\xi = (b_{ij}b_{jk}b_{ki}/6)^{1/3}$ and $\chi = (b_{ij}b_{ji}/2)^{1/2}$. Turbulence in the VDTT was nearly isotropic at high Reynolds numbers. The anisotropy of the turbulence in the soccer ball was adjustable, and each of the black squares corresponds to a different setting of the anisotropy. In the cases of the VKS and LEM, the cloud of points corresponds to measurements made at different positions near the centers of each apparatus.

the same moderate Reynolds number (it is the 4 bar data in Table I). The key point is that the shapes of the two spectra are nearly identical, down to the scale of the Dantec probe, $l_{trad.}$. This finding builds confidence in the NSTAP data. The deviation of their ratio from one, visible in the inset at the largest scales, is probably due to the usual problems with convergence at these scales, which are much longer than the integral scale. At scales smaller than the Dantec probe, or at large $k_1 l_{trad.}$, the ratio falls off. This roll-off indicates that the Dantec probe lost sensitivity relative to the NSTAP for $k_1 l_{trad.} > 1$. In addition to this spatial filtering effect, there are hints that temporal filtering of the hot-wire system can influence the measurement at high frequencies⁶². Most recent studies in pipe flows show that the frequency response of different anemometer/probe combinations can vary substantially⁶³. This ongoing work will need careful consideration.

Figure 29 shows the same spectra as in Fig. 27, but in the Kolmogorov variables. The inertial range is the approximate plateau in the curves. With increasing Reynolds number,

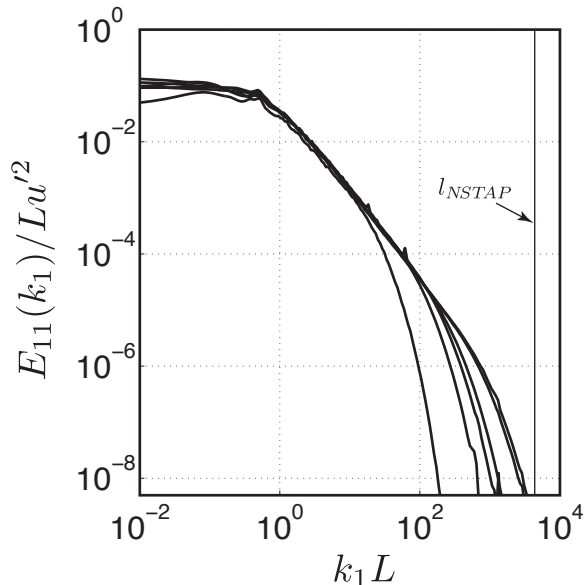


FIG. 27. The extension of the inertial range toward smaller scales with increasing Reynolds number. The curves correspond to the data summarized in table I, with the Reynolds number increasing from left to right as one follows the intersections of the curves with abscissa. The velocity and length scales, u' and L , respectively, were approximately the same for all experiments. The vertical bar marked l_{NSTAP} corresponds to the size of the probe, $30 \mu\text{m}$.

the so-called bottleneck, or the bump on the right side of the inertial range, grows more pronounced. However, it seems to lose prominence at the highest Reynolds numbers. The overall slope of the spectra in the inertial range grows more shallow with increasing Reynolds number, as has been observed before⁶⁴.

F. Scale Separation

Figure 30 shows the ratio of the integral scale, L , to the Kolmogorov scale, η . The integral scale is a measure of the size of the sweeping, energy containing motions, while the Kolmogorov scale measures the scale of the sharp, dissipative gradients. As mentioned in the introduction, higher Reynolds numbers are related to increased separation between these large and small scales. This expression can be made more precise. Using the relation $\epsilon \approx u'^3/L$, it is easy to show that $L/\eta \sim R_\lambda^{3/2}$. The line in the figure is a $3/2$ power law

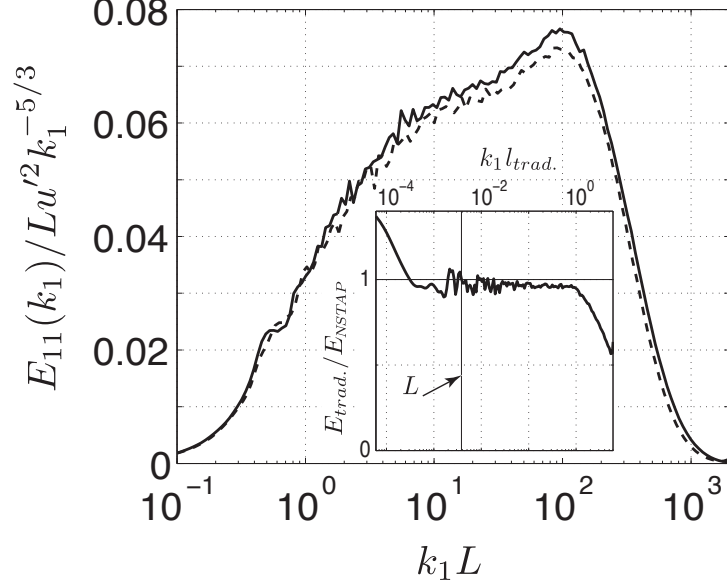


FIG. 28. A comparison of a spectrum acquired with an NSTAP (E_{NSTAP}) to one acquired with a standard Dantec hot wire ($E_{trad.}$). These data were acquired at 4 bar, so that the Taylor Reynolds number was about 730. The inset shows the ratio of the two spectra, which is approximately constant throughout the inertial range, and down to the scale that corresponds to the size of the Dantec hot wire probe, $l_{trad.} = 450 \mu\text{m}$. At smaller scales, the Dantec wire was less sensitive than the NSTAP. The vertical bar corresponds to the integral scale, L .

of arbitrary amplitude, and it follows the data reasonably well. This illustrates one of the chief advantages of the tunnel, which is that scale separation can be achieved by changing the pressure in the tunnel, and so by modulating the small scales alone. In this way, we separate the influence of scale separation on the small-scale dynamics from the influence of changes in the large-scale structure of the flow.

IV. CONCLUSION AND OUTLOOK

The new high-pressure, high-turbulence wind tunnel in Göttingen, the VDTT, makes experimental measurement of the structure and dynamics of nearly homogeneous and shearless turbulence possible at higher Reynolds numbers than before in its configuration at the time of writing. With passive grids we reach Taylor Reynolds numbers of 1600, whereas comparable studies reach about 870 (with an active grid)⁶⁵. To characterize the quality of

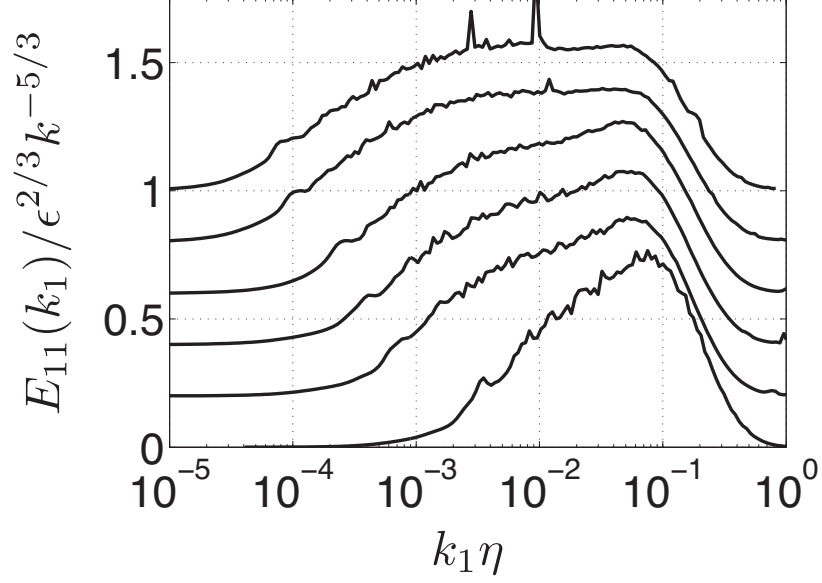


FIG. 29. Compensated spectra. As in Fig. 27, the data correspond to those summarized in Table I. The spectra are shifted vertically by 0.2 in order to set them apart, with the lowest Reynolds number data at the bottom. The extension of the inertial range is visible, as is the flattening of the spectra with increasing Reynolds number.

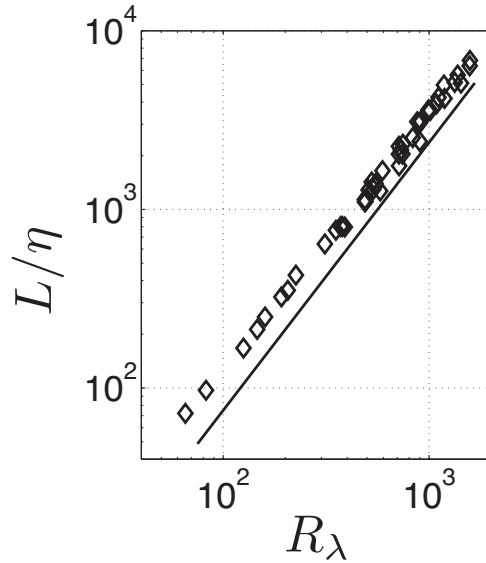


FIG. 30. Scale separation arises as the Reynolds number increases. Here we include data acquired at other pressures and fan speeds than included in the previous graphs or Table I. The solid line is a 3/2 power law, as discussed in the text.

TABLE II. Parameters predicted for the turbulence created by an active grid in the VDTT. The first line contains preliminary measurements made in a separate wind tunnel at a distance $d = 9$ m downstream of the active grid designed for the VDTT. The next lines are extrapolations based on these measurements to conditions in the VDTT. First, we assume that the turbulence intensity and dissipation rate will remain constant, and in the last line, we make an educated guess of what the VDTT might produce at the upstream end of a test section after optimization of the active grid.

Working Pressure		ρ	ν	U	d	u'/U	ϵ	R_λ	η	τ_η
fluid	[bar]	[kg/m ³]	10^{-6} [m ² /s]	[m/s]	[m]	[%]	[m ² /s ³]		[μ m]	[ms]
Air	1	1.29	14.0	11	9	6	0.46	620	280	5.5
Air	1	1.29	14.0	5.0	9	6	0.045	430	500	18
SF ₆	1	5.86	2.64	5.0	9	6	0.045	1000	140	7.7
SF ₆	15	107	0.15	5.0	9	6	0.045	4200	17	1.8
SF ₆	15	107	0.15	5.0	2	20	1.5	8000	6.9	0.32

the flow, hot-wire measurements were made behind a classical grid turbulence generator. Using tools that we describe in the paper, we will in the future reach even higher Reynolds numbers and introduce new Lagrangian measurement techniques.

With the addition of the active grid in the VDTT, we expect to reach Reynolds numbers before attainable only in the atmospheric boundary layer⁶⁶. That is, we will produce steady homogeneous and isotropic conditions, whereas existing data were acquired in unsteady inhomogeneous and anisotropic flows. As can be seen in Table II, very high Reynolds numbers up to R_λ at least 4200 will be possible with the active grid. These estimate is based on our initial experience with the new active grid in an open-circuit air tunnel, which we will publish separately, and where measurements were made at the downstream end of the tunnel. The Reynolds number will be higher at the upstream ends of the test sections, though the decay of Reynolds number with distance from the grid is typically slow⁶⁷. Further optimization of the active grid may yield yet higher Reynolds numbers, as has been observed with other active grids⁶⁸. In this way, we may reach Reynolds numbers up to 8000.

With the addition of the linear motor and camera system, the Lagrangian properties of the turbulence in the VDTT will become accessible. The Lagrangian approach coupled with

conventional Eulerian measurements under well-controlled conditions will provide a new perspective on fundamental turbulence questions. With its special properties the VDTT will make possible experiments in a well-understood and well-controlled flow at the highest turbulence levels yet possible in the laboratory, and with measurable spatial and temporal scales of motion. Therefore, it will make it possible to address problems important to environmental, atmospheric, and ocean sciences, to engineering and astrophysics.

ACKNOWLEDGMENTS

The project was initiated by Eberhard Bodenschatz, who led the project over the last ten years. His contribution starts with convincing investors through his fundamental questions about turbulence, and extends through the whole project to the present. The initial design study was prepared by Mickaël Bourgoïn and Eberhard Bodenschatz in 2004. Stefan Luther later also helped with these parameter calculations. Since then, several people and companies have contributed in ways that we outline here.

Each of the authors of this paper have participated in the tunnel design, the realization and the exploitation of the tunnel during the last ten years since the first initial design studies. Haitao Xu and Holger Nobach supervised the process from the specification of the VDTT's features until the inauguration of a working facility. Gregory Bewley and Michael Sinhuber made the facility into a scientific instrument, by performing the necessary optimization of its turbulent flow and developing measurement techniques.

The facility was designed by TLT Turbo GmbH, Zweibrücken, Germany. The pressure vessel was manufactured by Ludwig Elkuch AG, Bendorf, Liechtenstein. The gas handling system was designed, built, and installed by DILO Armaturen und Anlagen GmbH, Babenhausen, Germany. Financial support was provided by the Volkswagen Stiftung and the Max Planck Society. The design of the experimental hall, where the VDTT is located, was deeply influenced by the requirements of the VDTT. Siegfried Maier coordinated the interrelationship between the designs of each. He also participated in negotiations with companies and oversaw compliance with rules.

Udo Schminke and his colleagues in the mechanical workshop of the Max Planck Institute (MPIDS) provided their experience to the construction details of the VDTT. Many parts of the VDTT have been machined by them and in various ways they participated

intensively in the installation of the VDTT and especially of its internal parts, including the grids. Technicians at the MPIDS Andreas Renner, Andreas Kopp and Artur Kubitzek also contributed substantially to the design, installation, and regular maintenance of both the facility itself and of experimental apparatus. Bernhard Krey and his colleagues from management engineering participated directly in the installation of the tunnel.

Günter Schewe and Helmut Eckelmann helped to identify and solve problems with the flow and vibration in the tunnel. Visiting student Andrea Costanzo helped diagnose the flow separation that occurred in the expansion upstream of the upper test section. Visiting student Florent Lachaussée and Professor Greg Voth made with Gregory Bewley the measurements of active grid turbulence that we report here.

Measurements with adequate resolution were made possible through collaboration with Margit Vallikivi, Marcus Hultmark, and Lex Smits at Princeton University. They manufactured the NSTAPs that we used, and have been a vital resource in their proper use. We look forward to further fruitful collaboration with them, as we continue to explore turbulence with the VDTT.

REFERENCES

- ¹M. Vallikivi, M. Hultmark, S. C. C. Bailey, and A. J. Smits, *Exp. Fluids* **51**, 1521 (2011).
- ²S. Corrsin, *American Scientist* **49**, 300 (1961).
- ³M. Roth, *Q. J. R. Meteorol. Soc.* **126**, 941 (2000).
- ⁴A. J. Arnfield, *International Journal of Climatology* **23**, 1 (2003).
- ⁵I. D. James, *Environmental Modeling and Software* **17**, 363 (2002).
- ⁶R. A. Shaw, *Annu. Rev. Fluid Mech.* **35**, 183 (2003).
- ⁷S. B. Pope, *Proc. Combustion Institute* **34**, 1 (2013).
- ⁸D. W. Bechert, M. Bruse, W. Hage, and R. Meyer, *Naturwissenschaften* **87**, 157 (2000).
- ⁹C. H. Gibson, *Appl. Mech. Rev.* **49**, 299 (1996).
- ¹⁰D. Ryu, H. Kang, J. Cho, and S. Das, *Science* **320**, 909 (2008).
- ¹¹G. Ahlers, S. Grossmann, and D. Lohse, *Rev. Mod. Phys.* **81**, 503 (2009).
- ¹²E. Lindborg, *Geophysical Research Letters* **32**, L01809 (2005).
- ¹³J. A. Krommes, *Physics Reports* **360**, 1 (2002).
- ¹⁴L. Antiga and D. A. Steinman, *Biorheology* **46**, 77 (2009).

- ¹⁵N. Peters, *Turbulent Combustion* (Cambridge University Press, Cambridge, United Kingdom, 2000).
- ¹⁶L. Biferale and I. Procaccia, Phys. Rep. **414**, 43 (2005).
- ¹⁷G. I. Taylor, Proc. Roy. Soc. London. Series A, Math. Phys. Sci **151**, 421 (1935).
- ¹⁸G. Comte-Bellot and S. Corrsin, J. Fluid Mech. **25**, 657 (1966).
- ¹⁹U. Frisch, *Turbulence* (Cambridge University Press, Cambridge, United Kingdom, 1996).
- ²⁰S. C. C. Bailey, G. J. Kunkel, M. Hultmark, M. Vallikivi, J. P. Hill, K. A. Meyer, C. Tsay, C. B. Arnold, and A. J. Smits, J. Fluid Mech. **663**, 160 (2010).
- ²¹M. Munk, “On a new type of wind tunnel,” Technical Note 60 (National Advisory Committee for Aeronautics, 1921).
- ²²K. Oswatitsch and K. Wieghardt, Annual Review of Fluid Mechanics **19**, 1 (1987).
- ²³M. M. Munk and E. W. Miller, “The Variable Density Wind Tunnel of the National Advisory Committee for Aeronautics,” Tech. Rep. 227 (Langley Memorial Aeronautical Laboratory, 1926).
- ²⁴E. N. Jacobs and I. H. Abbot, “The N. A. C. A. Variable-Density Wind Tunnel,” Tech. Rep. 416 (National Advisory Committee for Aeronautics, 1933).
- ²⁵A. E. von Doenhoff and F. T. J. Abbott, “The Langley Two-Dimensional Low-Turbulence Pressure Tunnel,” Technical Note 1283 (Langley Memorial Aeronautical Laboratory, 1947).
- ²⁶R. J. McGhee, W. D. Beasley, and J. M. Foster, “Recent Modifications and Calibration of the Langley Low-Turbulence Pressure Tunnel,” Technical Paper 2328 (NASA, 1984).
- ²⁷M. M. Choudhari, M. G. Lockrad, D. P. Macaraeg, B. A. Singer, and C. L. Streett, “Aeroacoustic experiments in the Langley Low-Turbulence Pressure Tunnel,” Tech. Rep. (NASA, 2002).
- ²⁸http://crgis.ndc.nasa.gov/historic/Low_Turbulence_Pressure_Tunnel (2013).
- ²⁹R. C. Pankhurst, Nature **238**, 375 (1972).
- ³⁰H. Schlichting, “The Variable Density High Speed Cascade Wind Tunnel of the Deutsche Forschungsanstalt für Luftfahrt Braunschweig,” Tech. Rep. 91 (Advisory Group for Aeronautical Research and Development, 1956).
- ³¹C. B. Millikan, J. E. Smith, and R. W. Bell, Journal of the Aeronautical Sciences **15**, 69 (1948).
- ³²A. L. Kistler and T. Vrebalovich, J. Fluid Mech. **26**, 37 (1966).
- ³³E. Achenbach, J. Fluid Mech. **54**, 565 (1972).

- ³⁴H. Försting, E. Melzer, and G. Schewe, “Ein neuer Windkanal für gebäudeaerodynamische und -aeroelastische Untersuchungen bei Reynoldszahlen bis 10^7 ,” Tech. Rep. (DFVLR-AVA, 1981).
- ³⁵G. Schewe, Journal of Fluids and Structures **3**, 327 (1989).
- ³⁶G. Schewe, J. Fluid Mech. **133**, 265 (1983).
- ³⁷G. Schewe, J. Wind Eng. Ind. Aerodyn. **89**, 1267 (2001).
- ³⁸M. V. Zagarola and A. J. Smits, Physical Review Letters **78**, 239 (1997).
- ³⁹M. Hultmark, M. Vallikivi, S. Bailey, and A. J. Smits, Physical Review Letters **108**, 094501 (2012).
- ⁴⁰<http://www.princeton.edu/~gasdyn/Facilities/Facilities.html#SuperPipe> (2013).
- ⁴¹J. H. B. Hoogland, H. R. Van den Berg, and N. J. Trappeniers, Physica A **134**, 169 (1985).
- ⁴²R. L. Wilkins, J. Chem. Phys **51**, 853 (1969).
- ⁴³H. Goertler, Math. Phys. Klasse, Neue Folge **2** (1940).
- ⁴⁴W. R. Hawthorne, Proc. Roy. Soc. London. Ser. A. Math. Phys. Sci. **206**, 374 (1951).
- ⁴⁵G. B. Schubauer and W. G. Spangenberg, NACA Tech. Note , 1 (1948).
- ⁴⁶H. Makita, Fluid Dyn. Res. **8**, 53 (1991).
- ⁴⁷H. E. Cekli and W. van de Water, Exp. Fluids **49**, 409 (2010).
- ⁴⁸P. Knebel, A. Kittel, and J. Peinke, Exp. Fluids **51**, 471 (2011).
- ⁴⁹D. B. Blum *et al.*, New J. Physics **13**, 113020 (2011).
- ⁵⁰G. P. Bewley, *Using frozen hydrogen particles to observe rotating and quantized flows in liquid helium*, Ph.D. thesis, Yale University (2006).
- ⁵¹N. T. Ouellette, H. Xu, and E. Bodenschatz, Exp. Fluids **40**, 301 (2006).
- ⁵²W. Snyder and J. Lumley, J. Fluid Mech. **41**, 41 (1971).
- ⁵³Y. Sato and K. Yamamoto, J. Fluid Mech. **175**, 183 (1987).
- ⁵⁴S. Ayyalasomayajula, A. Gylfason, L. Collins, E. Bodenschatz, and Z. Warhaft, Phys. Rev. Lett. **97**, 144507 (2006).
- ⁵⁵R. A. Antonia and P. Burattini, J. Fluid Mech. **550**, 175 (2006).
- ⁵⁶G. P. Bewley, K. Chang, and E. Bodenschatz, Phys. Fluids **24**, 061702 (2012).
- ⁵⁷J. L. Lumley, Adv. Appl. Mech. **18**, 123 (1978).
- ⁵⁸S. B. Pope, *Turbulent Flows* (Cambridge University Press, Cambridge, England, 2000).
- ⁵⁹G. A. Voth, A. La Porta, A. M. Crawford, J. Alexander, and E. Bodenschatz, J. Fluid Mech. **469**, 121 (2002).

- ⁶⁰R. Zimmermann, H. Xu, Y. Gasteuil, M. Bourgoïn, R. Volk, J.-F. Pinton, and E. Bodenschatz, *Rev. Sci. Instru.* **81**, 055112 (2010).
- ⁶¹K. Chang, G. P. Bewley, and E. Bodenschatz, *J. Fluid Mech.* **692**, 464 (2012).
- ⁶²A. Ashok, S. Bailey, M. Hultmaark, and A. Smits, *Experiments in Fluids* **53**, 1713 (2012).
- ⁶³N. Hutchins, J. P. Monty, M. Hultmark, and A. Smits, “A direct measure of the frequency response of hot-wire anemometers,” Not yet published.
- ⁶⁴L. Mydlarski and Z. Warhaft, *J. Fluid Mech.* **320**, 331 (1996).
- ⁶⁵X. Shen and Z. Warhaft, *Phys. Fluids* **14**, 370 (2002).
- ⁶⁶B. R. Pearson and R. A. Antonia, *J. Fluid Mech.* **444**, 343 (2001).
- ⁶⁷P.-Å. Krogstad and P. A. Davidson, *J. Fluid Mech.* **642**, 373 (2010).
- ⁶⁸R. E. G. Poorte and A. Biesheuvel, *J. Fluid Mech.* **461**, 127 (2002).